Supplement of Earth Syst. Sci. Data, 18, 8149–8165, 2026
https://doi.org/10.5194/essd-18-8149-2026-supplement
© Author(s) 2026. CC BY 4.0 License.



Open Access Earth System Science Data

*Supplement of*

# Daily global sea surface ageostrophic current dataset from 1993–2023 via physics-informed deep learning

**Guangxi Cui et al.**

*Correspondence to:* Zhongya Cai (zycai@um.edu.mo)

The copyright of individual parts of the supplement might differ from the article licence.

Table S1. Hyperparameters and training configurations of the AC-PIDNN model.

| **Category** | **Hyperparameter / Setting** | **Value / Description** |
|---|---|---|
| Network Configuration | Optimizer | Adam |
| | Weight Initialization | Xavier |
| | Activation Function | Tanh |
| Regularization (to prevent overfitting) | Dropout Rate | 0.3 |
| | L2 Regularization Factor (λ) | 0.01 |
| Stage 1: Initialization (Quickly fit geostrophic current) | Loss Function | $Loss_{data}$ |
| | Learning Rate | 0.001 |
| | Epochs | 1000 |
| Stage 2: Transition (Gradually introduce physical constraints) | Loss Function | $Loss_{hybrid}$ |
| | Hybrid Loss Proportion | 1:1 |
| | Learning Rate | 0.0001 |
| | Epochs | 1000 |
| Stage 3: Physics-Informed (Minimize momentum equation residuals) | Loss Function | $Loss_{physics}$ |
| | Learning Rate | 0.00001 |
| | Epochs | 10000 |

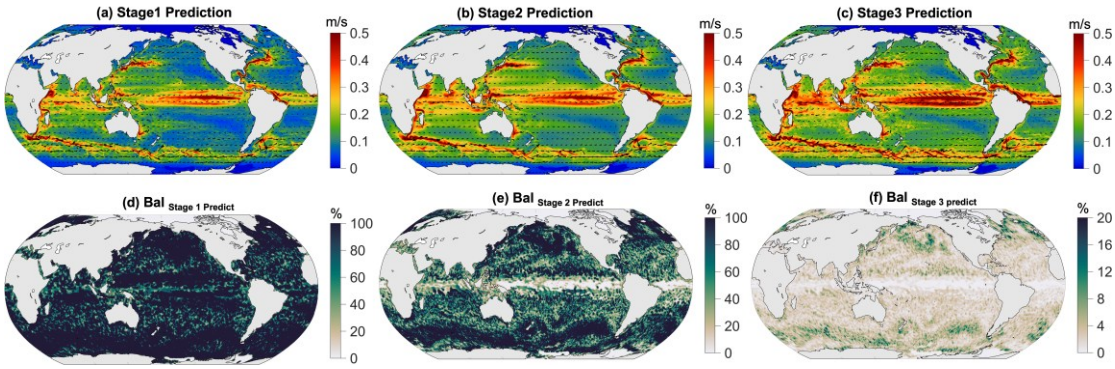



Figure S1. (a) Mean output current field of AC-PIDNN Stage 1 in 2021; (b) Mean output current field of AC-PIDNN Stage 2 in 2021; (c) Final mean output current field of AC-PIDNN Stage 3 in 2021; (d) Momentum balance (Bal) results for Stage 1; (e) Momentum balance (Bal) results for Stage 2; (f) Momentum balance (Bal) results for Stage 3.

To quantify the precise contribution of the physics-informed loss function within the neural network's training pipeline, a dedicated ablation study was conducted utilizing global flow field data from the year 2021. This experiment isolated the different loss constraints to evaluate their impact on both dynamical consistency and observational accuracy. The model was re-trained using the 2021 dataset, and the daily predicted surface currents were extracted across three distinct training phases: Stage 1 (representing the data-loss-only baseline), Stage 2 (hybrid loss optimization), and Stage 3 (the fully physics-constrained final model). By comparing these intermediate outputs against both theoretical momentum balance metrics (Bal) and station-based observational errors, the value added by the physical constraints beyond pure data-driven mapping can be systematically delineated.

A primary objective of integrating a Physics-Informed Neural Network (PINN) architecture is to ensure that the reconstructed ocean surface currents adhere to the governing physical laws of ocean dynamics, rather than merely minimizing the statistical error against remote sensing observations. As illustrated in Figures S1(a)–(c), the annual mean surface current fields generated by the AC-PIDNN model during Stages 1, 2, and 3 exhibit a stark contrast in dynamical consistency when evaluated alongside their corresponding momentum balance residuals (Figures S1(d)–(f)). Because the initial Stage 1 relies exclusively on data loss without any embedded physical constraints, the neural network acts as a standard data-fitting algorithm. Consequently, the output entirely lacks momentum balance correction, leading to severe dynamical inconsistencies where the momentum residuals exceed 100% across the vast

majority of the global ocean regions. Upon introducing a hybridized loss function in Stage 2 that begins blending physical constraints with observational data, a dramatic correction in the flow field's dynamical structure is observed, with the global mean momentum residual dropping precipitously to approximately 51%. In the final Stage 3, the output is rigorously constrained by the complete physics loss. This proper parameterization forces the reconstructed flow field to obey the fundamental equations of motion, vastly improving the momentum balance and reducing the global average momentum residual to a mere 1.2%. This progression unequivocally demonstrates that the physics-informed stages provide a profound improvement extending well beyond initial data fitting. The physics loss serves as a critical mechanism that enforces strict physical consistency, thereby ensuring the hydrodynamic reliability of the reconstructed surface currents.

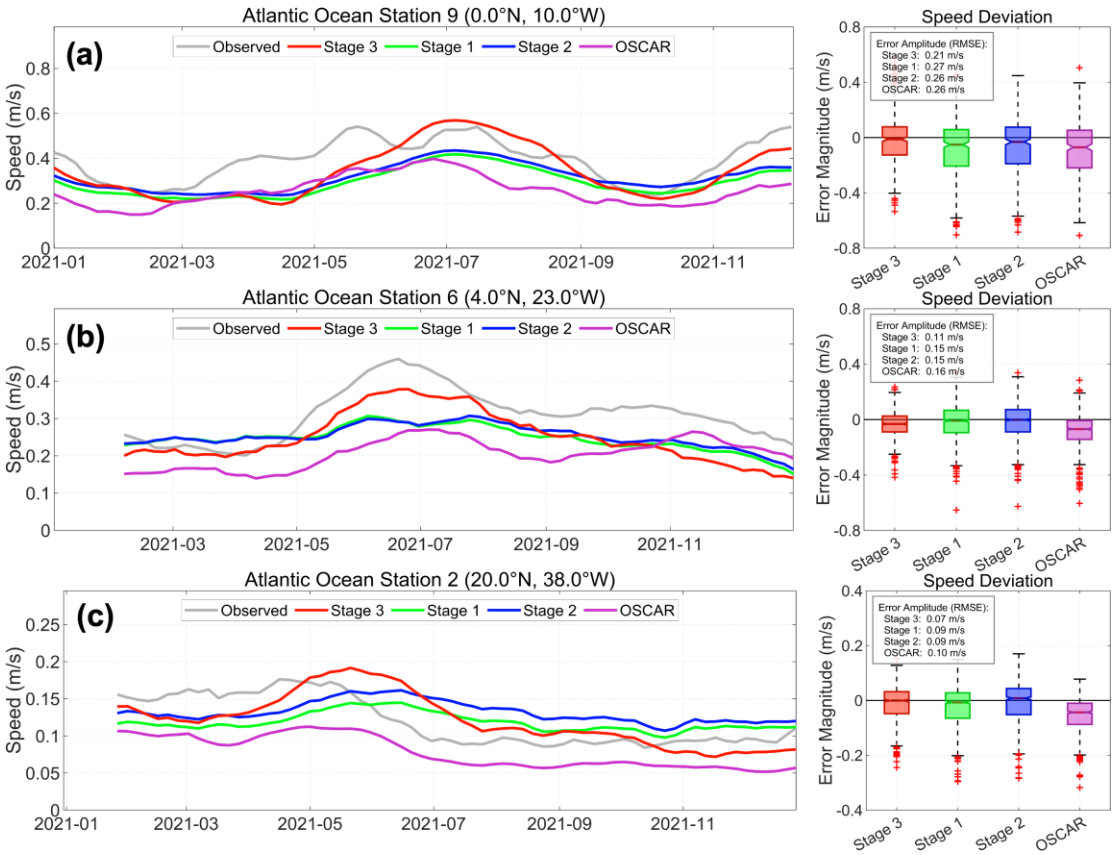



**Figure S2.** Comparison of the output current fields from the three training stages of AC-PIDNN and OSCAR product velocities against in-situ observational data.

To confirm that this improved dynamical balance translates to real-world accuracy, the outputs

of all three training stages, alongside the standard OSCAR product, were further evaluated against independent in-situ mooring data. Focusing on the velocity time series from successfully matched observation stations in 2021, the progressive incorporation of physical laws was shown to systematically refine the accuracy of the modeled velocities. The average errors were recorded as 0.17 m/s for Stage 1, 0.16 m/s for Stage 2, and 0.13 m/s for Stage 3, compared to 0.17 m/s for the OSCAR product. The data clearly indicate that the Stage 3 output aligns most closely with the in-situ measurements, significantly outperforming the Stage 1 baseline, the intermediate Stage 2 output, and the widely used OSCAR product. Purely data-driven approaches (Stage 1) remain highly susceptible to the inherent noise and spatial gaps present in multi-source satellite altimetry and scatterometry data. By enforcing momentum conservation, the subsequent physics-informed stages effectively filter out dynamically impossible artifacts, preventing overfitting to observational noise and yielding a flow field that is both physically coherent and statistically more accurate. This direct comparison firmly substantiates the superiority and absolute necessity of the physics-informed training stages within the AC-PIDNN framework.

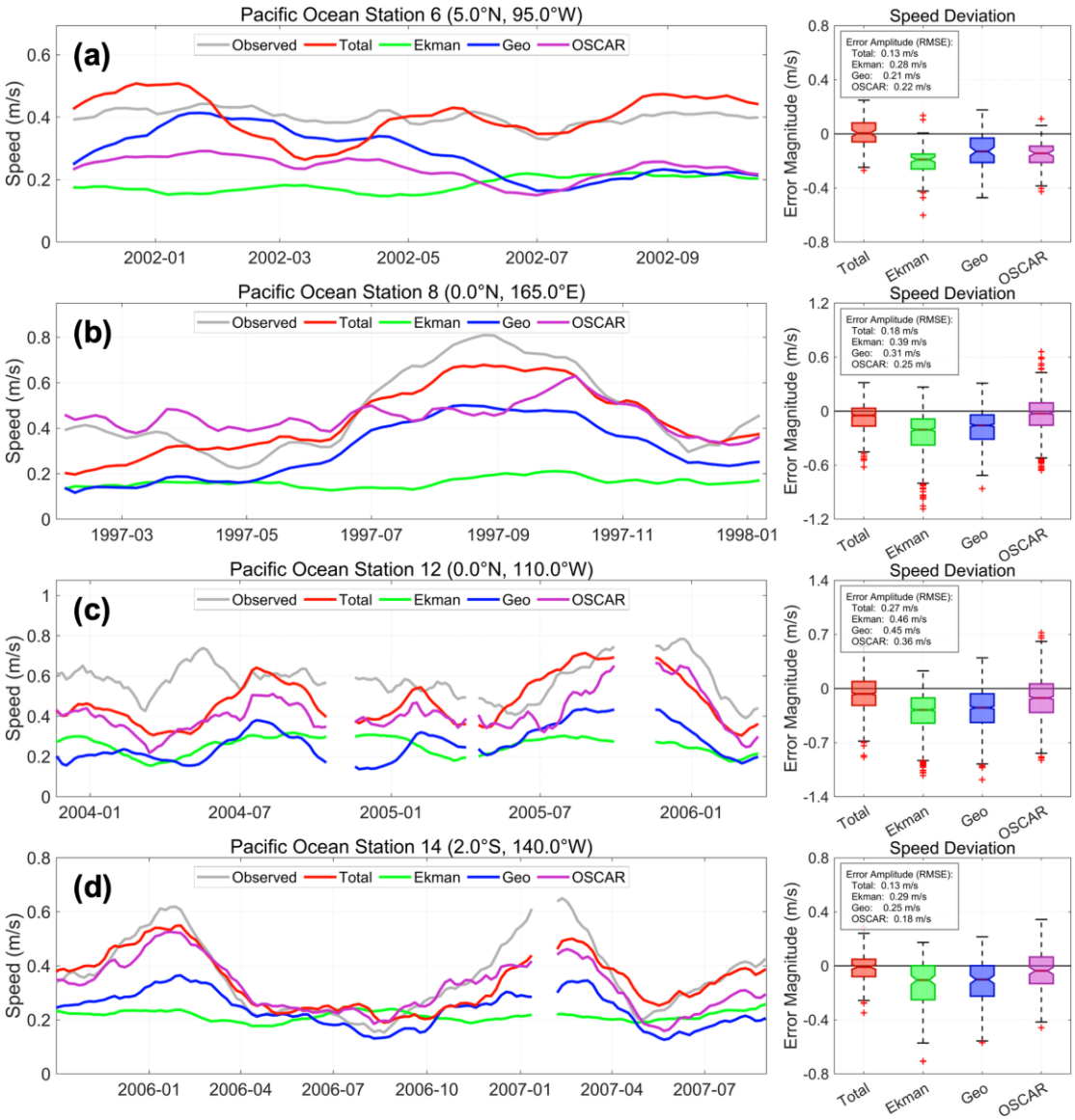



Figure S3. Time series curves of the AC-PIDNN-corrected flow field, geostrophic flow, Ekman flow, and OSCAR product flow field versus the measured data.

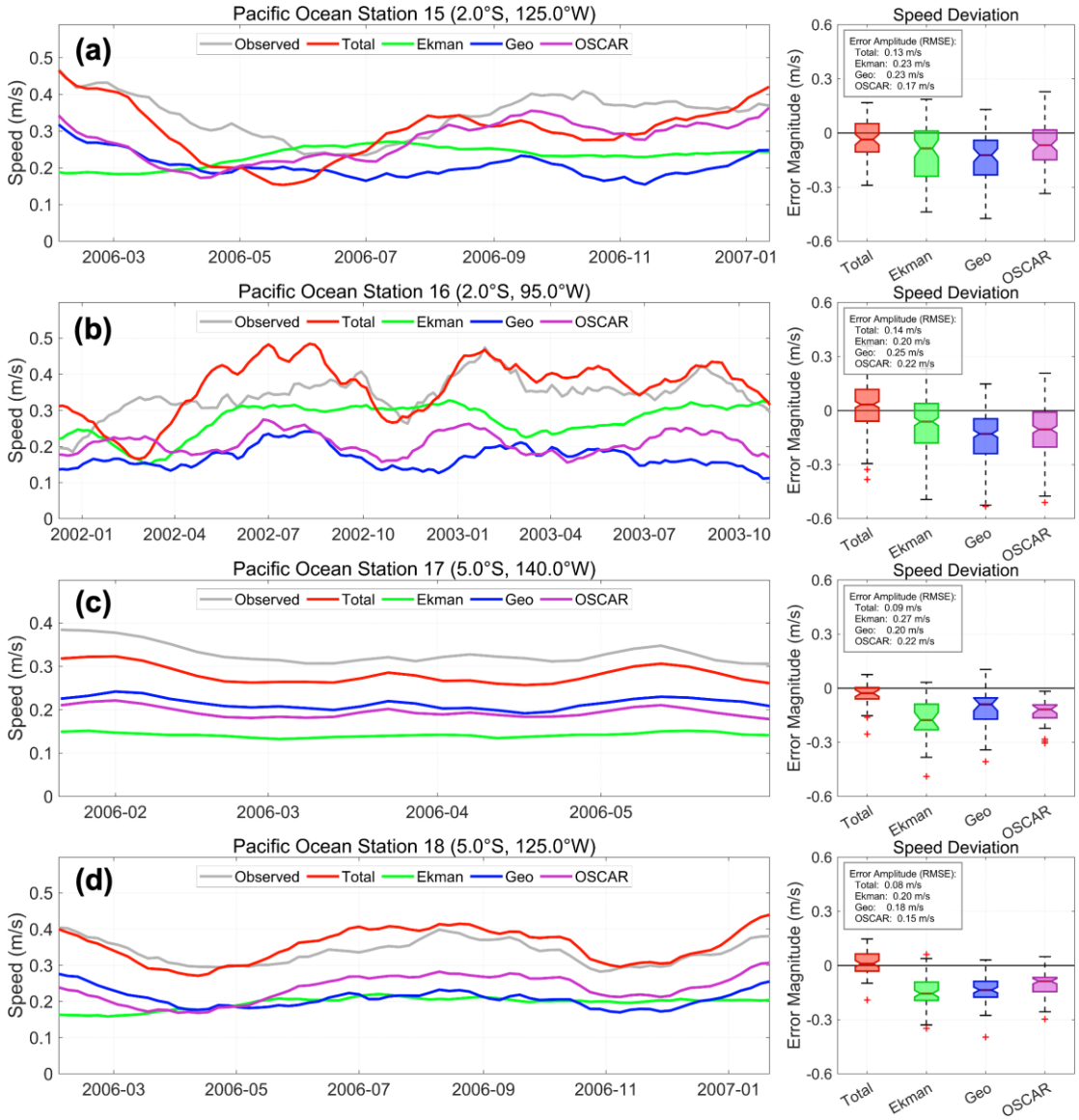



Figure S4. Time series curves of the AC-PIDNN-corrected flow field, geostrophic flow, Ekman flow, and OSCAR product flow field versus the measured data.

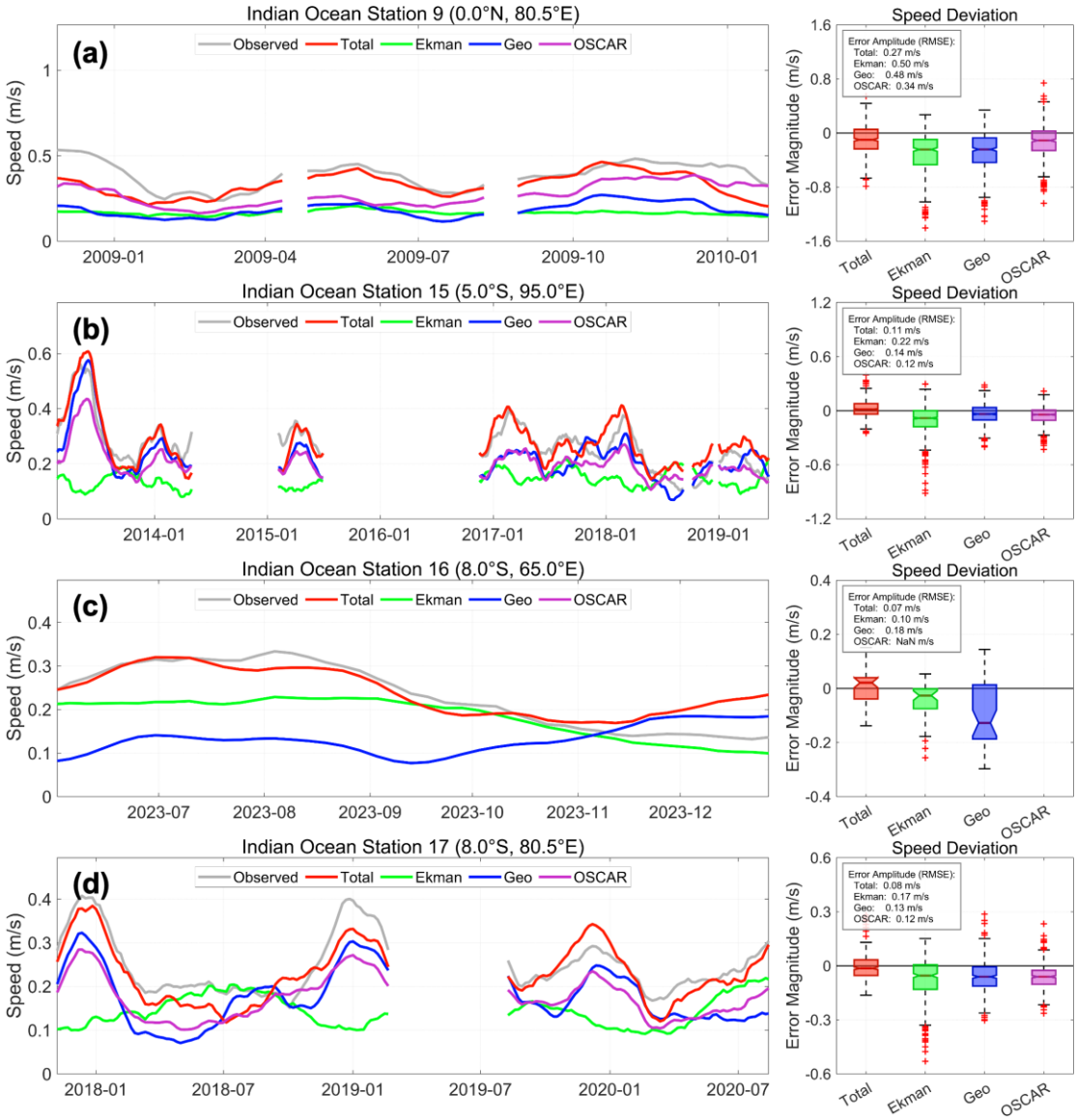



Figure S5. Time series curves of the AC-PIDNN-corrected flow field, geostrophic flow, Ekman flow, and OSCAR product flow field versus the measured data.

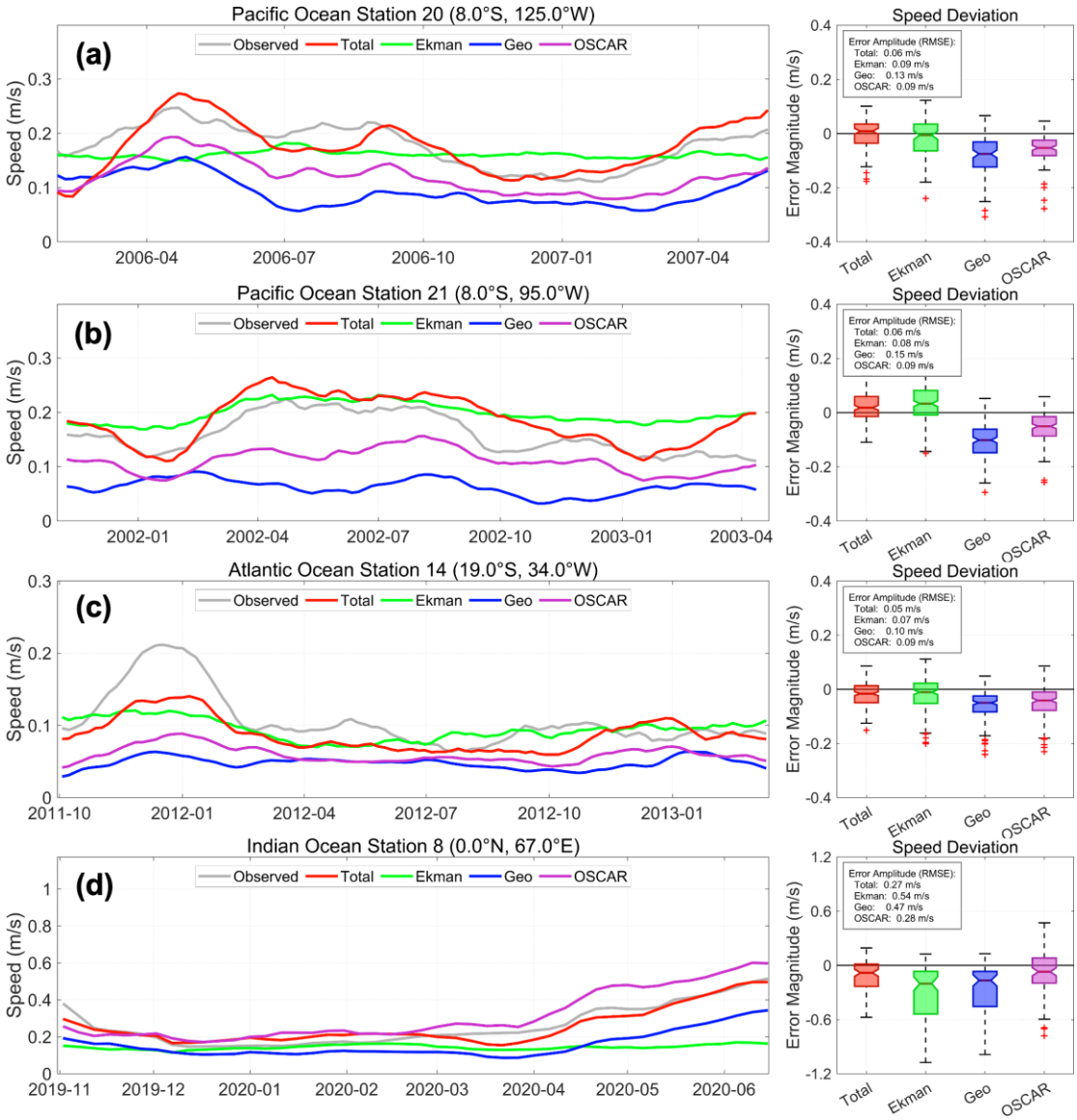



Figure S6. Time series curves of the AC-PIDNN-corrected flow field, geostrophic flow, Ekman flow, and OSCAR product flow field versus the measured data.

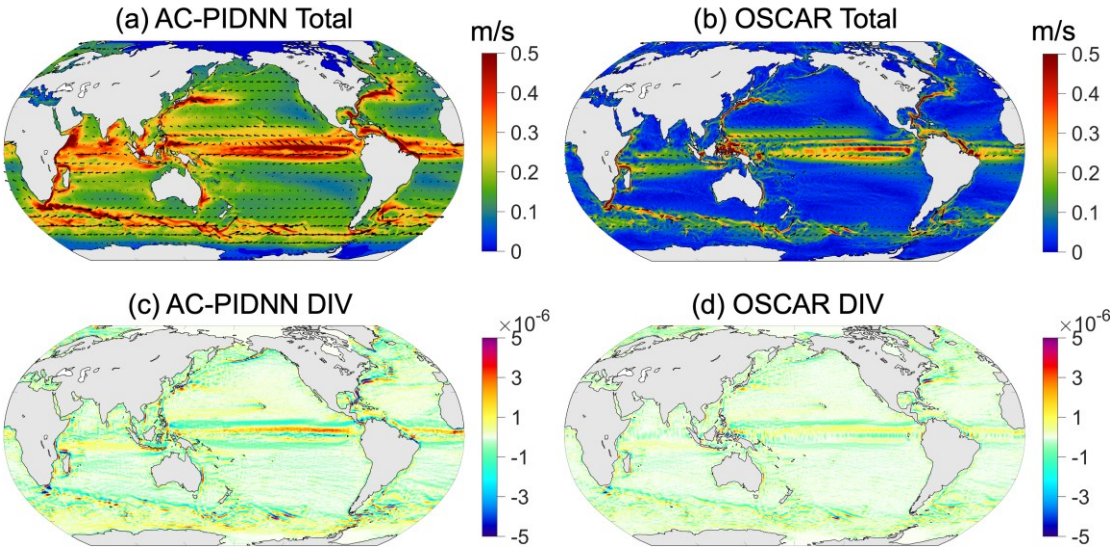



Figure S7. (a) 1993–2022 mean flow field from AC-PIDNN; (b) 1993–2022 mean flow field from the OSCAR product; (c) divergence of the 1993–2022 mean flow field from AC-PIDNN; (d) divergence of the 1993–2022 mean flow field from the OSCAR product.

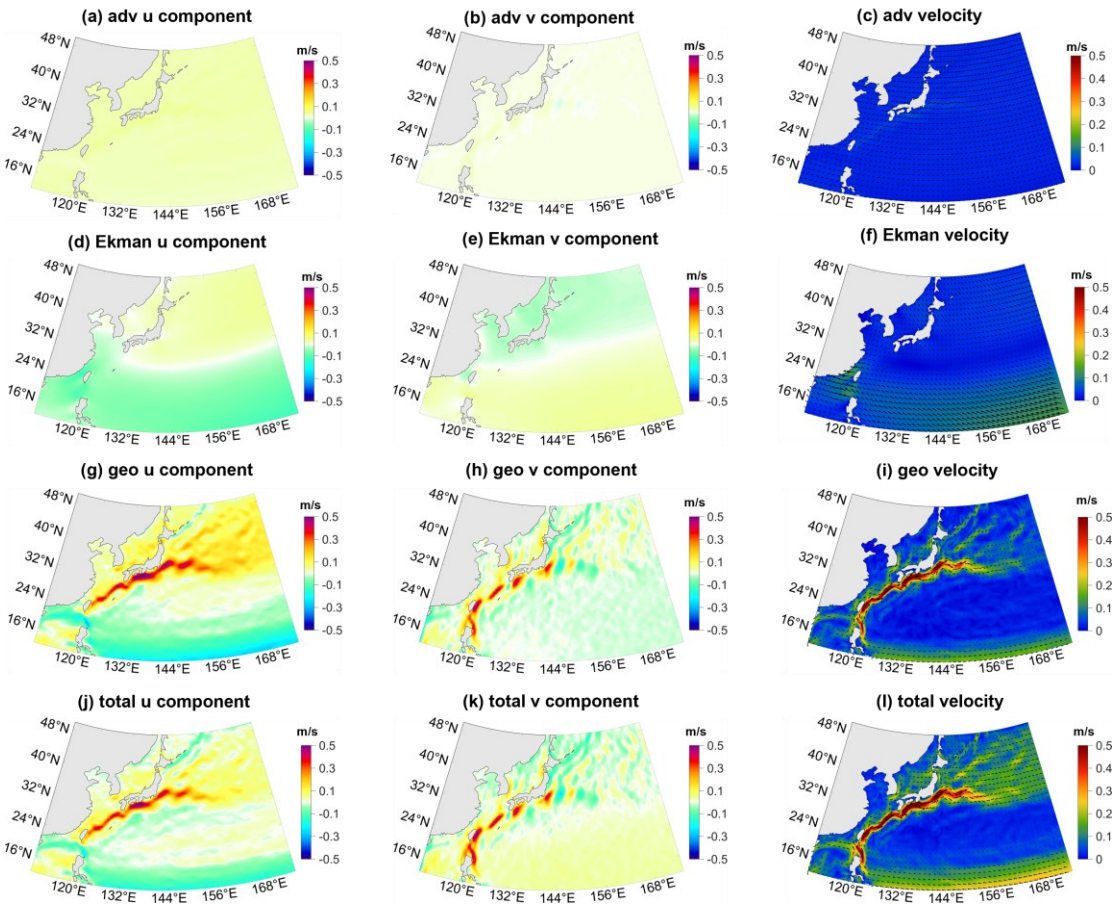



Figure S8: Results of sea surface circulation correction for the Kuroshio Current from 1993 to 2023, using the AC-PIDNN model. Panels (a)–(c) show the u-component, v-component, and flow field of the advective component; panels (d)–(f) show the u-component, v-component, and flow field of the Ekman component; panels (g)–(i) show the u-component, v-component, and flow field of the geostrophic component; panels (j)–(l) show the u-component, v-component, and flow field of the total circulation.

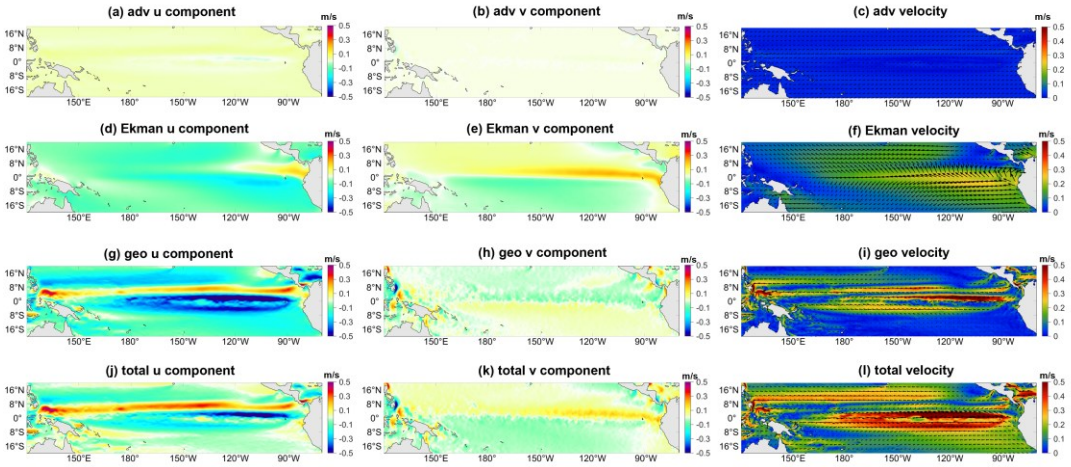



Figure S9: Results of sea surface circulation correction for the Equatorial Region from 1993 to 2023, using the AC-PIDNN model. Panels (a)–(c) show the u-component, v-component, and flow field of the advective component; panels (d)–(f) show the u-component, v-component, and flow field of the Ekman component; panels (g)–(i) show the u-component, v-component, and flow field of the geostrophic component; panels (j)–(l) show the u-component, v-component, and flow field of the total circulation.

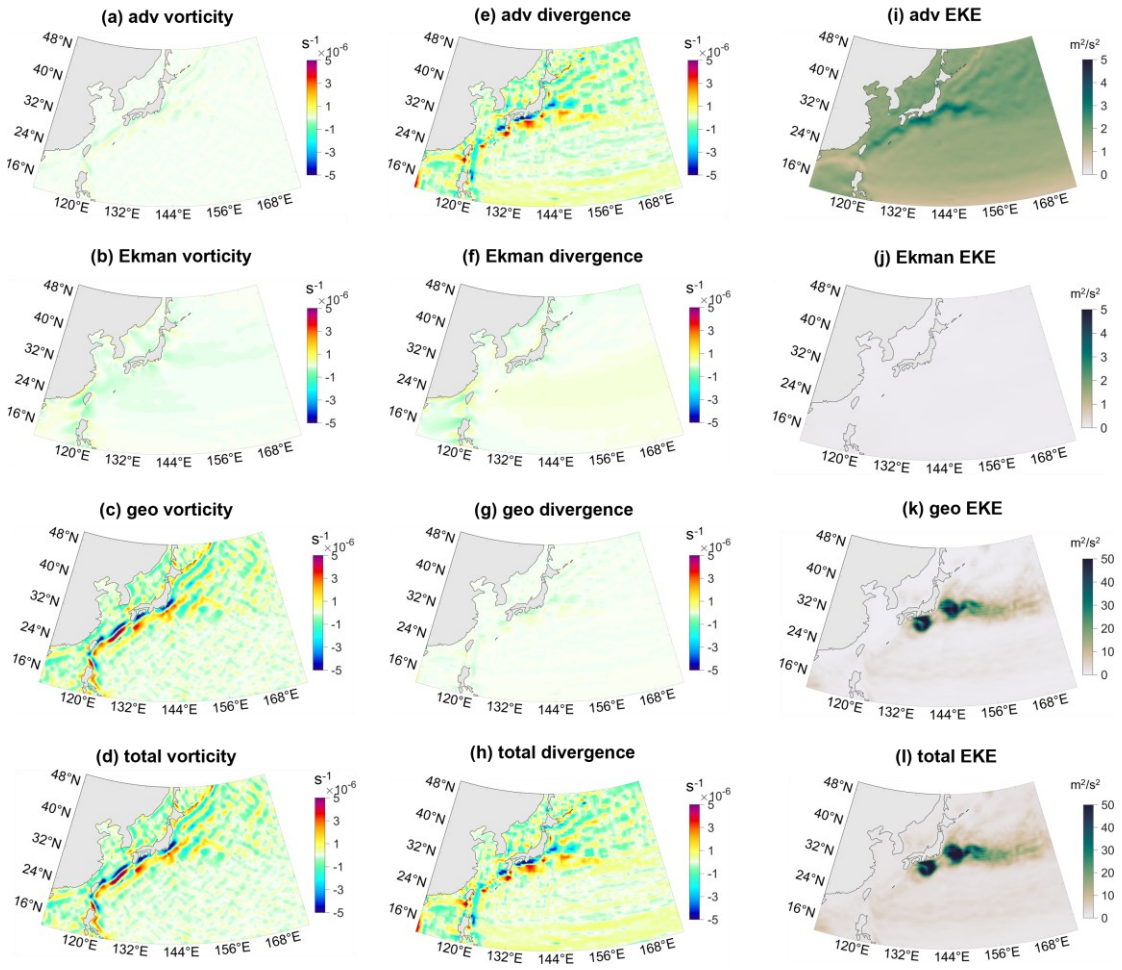



Figure S10: Characteristics of the dynamic parameters of the corrected 30-year average sea surface circulation in the Kuroshio Current. Panels (a)–(d) showing the vorticity of the advective, Ekman, geostrophic, and total components, respectively; panels (e)–(h) showing the divergence of the advective, Ekman, geostrophic, and total components, respectively; panels (i)–(l) showing the eddy kinetic energy (EKE) of the advective, Ekman, geostrophic, and total components, respectively.

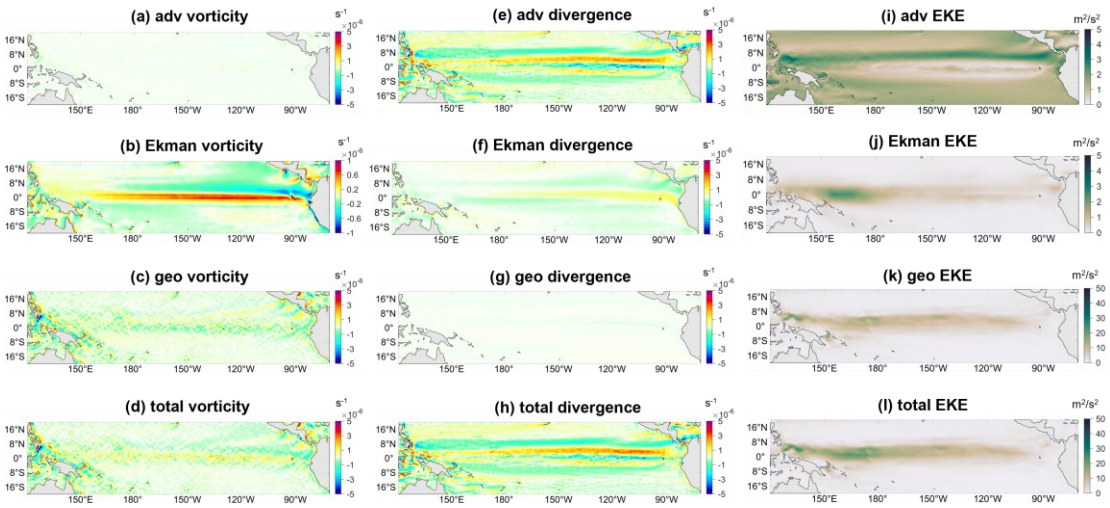



Figure S11: Characteristics of the dynamic parameters of the corrected 30-year average sea surface circulation in the Equatorial Region. Panels (a)–(d) showing the vorticity of the advective, Ekman, geostrophic, and total components, respectively; panels (e)–(h) showing the divergence of the advective, Ekman, geostrophic, and total components, respectively; panels (i)–(l) showing the eddy kinetic energy (EKE) of the advective, Ekman, geostrophic, and total components, respectively.